J. Fluid Mech. (2021), *vol*. 922, A33, doi:10.1017/jfm.2021.567

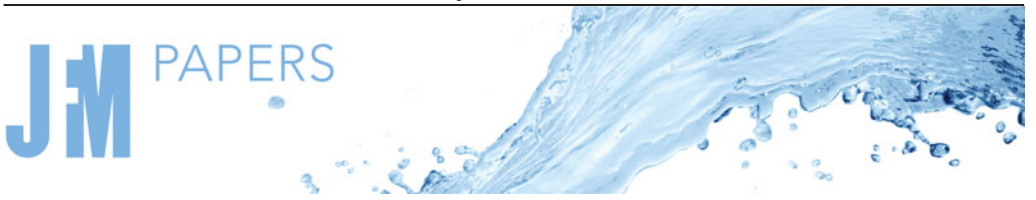

Travelling vortices over mountains and the long-term structure of the residual flow

Luis Zavala Sansón[1],† **and Jeasson F. Gonzalez**[1]

[1]Departamento de Oceanografía Física, CICESE, Carretera Ensenada-Tijuana 3918, 22860 Ensenada, Baja California, México

(Received 14 August 2020; revised 21 May 2021; accepted 18 June 2021)

In the context of rotating geophysical flows, the presence of variable topography affects the motion of intense vortices and promotes the generation of new vortical structures. In this study, the quasi-two-dimensional dynamics of such systems is examined with numerical simulations and analytical models. The results are discussed from two points of view. First, the motion of a barotropic, dipolar vortex encountering a submarine mountain is analysed, with an emphasis on the modification of the trajectory and dipole structure when passing over the topography. For relatively low mountains, the vortex path is deflected towards the anticyclonic side of the dipole owing to squeezing effects (as the anticyclone becomes more intense than the cyclonic part). For higher mountains, the dipole splits into two parts; the anticyclone pairs with newly formed positive vorticity (generated by the stretching fluid moving downhill), while the cyclone remains trapped near the summit. These results are discussed using modulated point-vortex models. Second, the long-lived residual flows over the topography are studied. The most conspicuous cases are asymmetric dipolar vortices, which remain confined on the summit while rotating clockwise. The formation of new dipoles arises from the combination of nonlinear motions and topographic Rossby waves around the mountain. The results are illustrated with new analytical solutions of nonlinear dipoles over mountains.

Key words: vortex dynamics, topographic effects, rotating flows

1. Introduction

When considering a homogeneous fluid layer in a rotating system, the flow can be described in terms of vertical columns aligned with local gravity, as predicted by the Taylor–Proudman theorem and observed in rotating tank experiments since the early works of Taylor (1921). This phenomenon occurs for a sufficiently small Rossby number, defined as the ratio of the system's rotation period (one day) and the time scale of the

† Email address for correspondence: lzavala@cicese.mx

flow (Pedlosky 1987; Vallis 2017). Thus, columnar motion is observed for rapidly rotating systems or, equivalently, flows with sufficiently long time scales (of the order of several days). Because the horizontal flow is depth-independent (outside boundary layers), the dynamics are usually represented using two-dimensional (2-D) models (Hopfinger & van Heijst 1993).

In the presence of bottom topography, the flow still moves in a columnar fashion, but becomes affected by stretching and squeezing effects as columns move across the topography. In such rotating systems vertical motions exist, but depend on the divergence/convergence of the horizontal flow. The dynamical effects of topography can be incorporated into quasi-2-D models. The most straightforward case is the quasi-geostrophic (QG) model, in which the topographic variations are much smaller than the average fluid depth (Carnevale *et al.* 1995). A more general quasi-2-D formulation is the shallow-water (SW) equations under the rigid-lid approximation (Grimshaw, Tang & Broutman 1994). In addition to the inclusion of variable topography, quasi-2-D models may incorporate bottom damping effects, such as the so-called Ekman friction associated with the thin boundary layer in rotating systems (Zavala Sansón & van Heijst 2002). A general review of quasi-2-D models with topography and several experimental examples has been reported by Zavala Sansón & van Heijst (2014). Geophysical flows in the oceans and in the atmosphere, with horizontal length scales of $O(100–1000)$ km and time scales of days, weeks or even months, are sufficiently slow to be strongly affected by the Earth's rotation and, eventually, by bottom topography. Therefore, quasi-2-D formulations are often applied for modelling geophysical vortices (Hopfinger & van Heijst 1993; van Heijst & Clercx 2009).

This study is motivated by two different oceanic phenomena: (i) the encounter of travelling dipolar vortices with a topographic obstacle, and (ii) the residual flow left over the topography. Regarding the first motivation, an illustrative observational example is the northwestward drift of the Agulhas rings, which travel through the South Atlantic Ocean and transit over the Walvis Ridge and the Mid-Atlantic Ridge (Schouten *et al.* 2000; Nencioli, Dall'Olmo & Quartly 2018). Monopolar vortices drift arises from the so-called β-effect associated with latitudinal variations of the planetary vorticity (van Leeuwen 2007). Dipolar vortices, on the other hand, consist of two counter-rotating vortices whose mutual interactions provide the self-propelling mechanism. Dipolar structures are well-known in classical 2-D formulations (Meleshko & van Heijst 1994), geophysical models (Flierl, Stern & Whitehead 1983) and field observations (Hughes & Miller 2017). Because travelling structures transport heat, momentum and passive properties, it is of interest to study the fate of the colliding dipolar vortex: whether it is destroyed, modified or unaffected during its passage over the topography.

Our second motivation is the residual flow or 'signature' left by the vortex over a topographic feature. Observational evidence has shown that mesoscale oceanic motions may be trapped over the tip of seamounts for several days or weeks (Beckmann & Mohn 2002; Trasviña-Castro *et al.* 2003). Because these structures remain coherent during that lapse of time, they may generate intense advection of nutrients and retain biological material, which favours the abundance of plankton and fish (Genin 2004). Here we explore with idealised models the generation of long-lived motions that arise when the fluid over the topography is perturbed.

Based on experimental and observational antecedents, we study the evolution of a barotropic flow over an isolated, submerged mountain on an f-plane from two points of view. First, we examine the encounter of a dipolar vortex with the submarine mountain.

The main purpose is to investigate the fate of the travelling dipole depending on the topographic parameters (height and width of the mountain). This approach follows the line of reasoning applied in several experimental studies on vortices over topography. For instance, monopolar cyclonic vortices over a weak linear topographic slope are induced to drift upslope and to the left (looking uphill), under the so-called topographic β-effect (Carnevale, Kloosterziel & van Heijst 1991; van Heijst 1994; Flór & Eames 2002). Steep slopes promote the formation of new vortices and oscillating jets (Zavala Sansón & van Heijst 2000; Sutyrin & Grimshaw 2010). Topographic steps may cause the deviation or 'reflection' of monopoles (Zavala Sansón, van Heijst & Doorschot 1999) and dipoles (Tenreiro, Zavala Sansón & van Heijst 2006; Hinds *et al.* 2009). When using an isolated topographic feature in the laboratory, the flow evolution strongly depends on the shape of the submerged obstacle. Experiments with monopolar vortices have been carried out using conical (Carnevale *et al.* 1991), cylindrical (Cenedese 2002) and Gaussian (Zavala Sansón, Barbosa Aguiar & van Heijst 2012) 'seamounts', as well as elongated ridges (Zavala Sansón 2002). To our knowledge, however, the case of a dipolar vortex encountering a submerged mountain has not been addressed. We will do so by using nonlinear SW simulations and also a point-vortex model modulated by topography.

The second strand in this study is the long-term evolution of the residual flow that remains trapped over the mountain. In this problem, the original dipole has moved away from the topography and therefore plays a secondary role. Long-lived motions over the summit can be regarded as the response of the flow dynamics before finite perturbations. Trapped structures over submarine obstacles are sometimes referred to as 'Taylor caps' because they are associated with the dynamical constraint of rotating fluids to move across isobaths (Chapman & Haidvogel 1992). Early works on this subject were developed during the 1960s and 1970s, as summarised by Verron & Le Provost (1985). Most of those studies were focused on QG uniform currents above an isolated mountain, which generate an anticyclone over the summit (owing to squeezing effects) and a cyclonic vortex at the lee side owing to stretching effects (Huppert & Bryan 1976). More recent analytical studies describe the structure and stability of monopolar vortices over seamounts (Nycander & Lacasce 2004; Ryzhov & Koshel 2013; Hinds, Johnson & McDonald 2016; Zhao, Chieusse-Gérard & Flierl 2019).

In the present study, in contrast, we examine the flow response over the mountain after being disturbed (by the passing of the original dipole) in SW simulations. The main results are related to two main phenomena: (*a*) the excitation of topographic Rossby waves that rotate clockwise around the mountain (for a positive Coriolis parameter) (Rhines 1969; Zavala Sansón 2010); and (*b*) the generation of nonlinear dipolar structures that rotate as a whole in the same direction. The formation of the latter was noted in the simulations by Verron & Le Provost (1985). More recently, asymmetric dipoles on submerged mountains were neatly observed in laboratory experiments, where the structures rotate around the topography during several inertial periods (Zavala Sansón *et al.* 2012). We will show that for sufficiently compact mountains, such dipoles are indeed the natural response before perturbations. Additionally, the characteristics of the dipoles (strength and angular speed around the mountain) will be discussed in terms of the nonlinear analytical solutions derived by Gonzalez & Zavala Sansón (2021).

The paper is organised as follows. In § 2, we present the dynamical model and the numerical methods, which includes an outline of the simulations. Section 3 is devoted to examining the modification of the structure and trajectory of dipoles passing over the

mountain. In § 4, we study the residual flow left over the summit at long times. Finally, in § 5, the results are summarised and discussed.

2. Dynamical model and numerical method

An appropriate dynamical model to represent the evolution of vortical structures in a rotating fluid with topography is the SW formulation. Here we describe the model equations and the procedure to solve them numerically.

2.1. *Quasi-2-D homogeneous flow over topography*

Consider a rapidly rotating system on an f-plane (with constant Coriolis parameter f_0), where the rotation axis is parallel to gravity. The motion of a homogeneous fluid is sufficiently slow to assume that the hydrostatic approximation holds in the vertical direction (Pedlosky 1987), which implies that the velocity components (u, v) in the horizontal plane (x, y) are independent of depth. Thus, the fluid motion is nearly two-dimensional (quasi-2-D). The thickness of the fluid layer $h(x, y)$ is space-dependent owing to the shape of the variable topography and time-independent by using the rigid-lid approximation. From the integrated continuity equation, the horizontal velocities may be defined in terms of a transport function $\psi(x, y, t)$ as

$$u = \frac{1}{h}\frac{\partial \psi}{\partial y}, \quad v = -\frac{1}{h}\frac{\partial \psi}{\partial x}. \tag{2.1a,b}$$

The vertical component of the relative vorticity is defined as $\omega(x, y, t) = \partial v/\partial x - \partial u/\partial y$. It is easily verified that

$$\omega = -\frac{1}{h}\nabla^2\psi + \frac{1}{h^2}\nabla h \cdot \nabla \psi, \tag{2.2}$$

where $\nabla^2 = \partial^2/\partial x^2 + \partial^2/\partial y^2$ is the Laplacian. The relative vorticity equation is

$$\frac{\partial \omega}{\partial t} + J\left(\frac{\omega + f_0}{h}, \psi\right) = \nu\nabla^2\omega, \tag{2.3}$$

where $J(a, b) = (\partial a/\partial x)(\partial b/\partial y) - (\partial a/\partial y)(\partial b/\partial x)$ is the Jacobian operator and ν is a viscous coefficient. In the context of laboratory experiments, ν is the molecular viscosity; for geophysical flows, this parameter is a turbulent coefficient. The potential vorticity is

$$q = \frac{\omega + f_0}{h}. \tag{2.4}$$

In the absence of viscous effects, the vorticity equation transforms into

$$\frac{\partial q}{\partial t} + u\frac{\partial q}{\partial x} + v\frac{\partial q}{\partial y} = 0, \tag{2.5}$$

which expresses the material conservation of q. Note that we will ignore any external forcing at the upper surface and friction effects at the solid bottom. Additionally, recall that the SW formulation admits significant depth changes owing to the topography, while the traditional QG model demands that such changes must be much smaller than the mean fluid depth (Grimshaw *et al.* 1994). For non-rotating systems ($f_0 = 0$), the dynamical model (2.1*a*,*b*)–(2.3) is equivalent to the 'lake equations' (see e.g. Camassa, Holm & Levermore 1997).

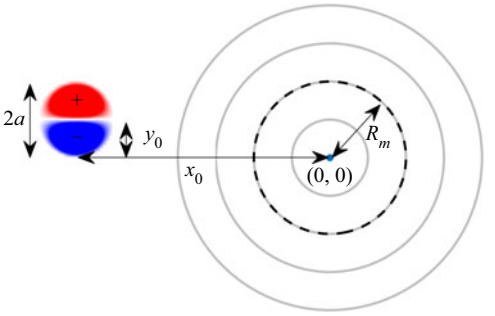

Figure 1. Experimental configuration. The submarine mountain (2.6) is represented with topography contours (grey circles) centred at the origin. The contours correspond to fluid depth $h(r)$ evaluated at radial distances $(0.5, 1, 1.5, 2)R_m$ (dashed contour corresponds to $h(R_m)$). The dipolar vortex has a radius a and is initially located to the left of the mountain $x_0 < 0$ at (x_0, y_0) (in this example $y_0 > 0$). Symbols $\pm$ indicate the vorticity sign at each half of the dipole.

2.2. *Topography and initial conditions*

We consider an axisymmetric submarine mountain centred at the origin. The topography has a Gaussian shape, such that the fluid depth is

$$h(r) = H - H_m \exp(-r^2/R_m^2), \tag{2.6}$$

where $r^2 = x^2 + y^2$, H is the maximum depth (away from the mountain), H_m is the height of the topography and R_m is its radial scale.

Using polar coordinates (r, θ), the initial dipolar condition is the well-known Chaplygin–Lamb vortex (Meleshko & van Heijst 1994), whose vorticity distribution inside a circle with radius a is

$$\omega(r, \theta) = -\frac{2Us_l}{a\mathrm{J}_0(s_l)}\mathrm{J}_1(s_l r/a)\sin\theta, \quad r \leqslant a \tag{2.7}$$

and $\omega = 0$ for $r > a$. Here, J_0 and J_1 are Bessel functions of the first kind. The constant $s_l = 3.8317$ is the smallest root of J_1, that is, $\mathrm{J}_1(s_l) = 0$. The dipole is symmetrical and travels along the positive x-direction at a constant speed $U > 0$. The initial position of the dipole is (x_0, y_0) with $x_0 < 0$, so the vortex approaches the submarine mountain. In some cases we explored the frontal collision ($y_0 = 0$) and in some others the dipole trajectory was not aligned with the mountain ($y_0 \neq 0$). Figure 1 shows a typical configuration in one of the experiments with $y_0 > 0$. Other useful quantities are the total energy per density (Zavala Sansón, van Heijst & Backx 2001)

$$E_0 = \frac{H}{2}\int_0^{2\pi}\int_0^a (u^2 + v^2) r\,\mathrm{d}r\,\mathrm{d}\theta = 2\pi H a^2 U^2, \tag{2.8}$$

and the circulation of the poles (Meleshko & van Heijst 1994)

$$\Gamma_0^{\pm} = \int_0^{2\pi}\int_0^a \omega^{\pm} r\,\mathrm{d}r\,\mathrm{d}\theta = \pm 6.83 Ua, \tag{2.9}$$

where symbols $+$ and $-$ indicate positive and negative values. Because the initial dipole is symmetric, we define $\Gamma_0 \equiv \Gamma_0^+ = |\Gamma_0^-|$.

Variable parameters	Symbol and identifier	Values		
y-initial position	y_0/a (A, B, C)	0 (frontal)	1 ('north')	−1 ('south')
Mountain height	H_m/H ($i = 1, 2, 3$)	0.1 (low)	0.3 (medium)	0.5 (tall)
Mountain radius	R_m/a ($j = 1, 2, 3$)	1 (narrow)	2 (medium)	3 (wide)

Table 1. Outline of the 27 numerical simulations. The sets of experiments are identified according to a matrix nomenclature: for instance, experiment A_{11} corresponds to $y_0/a = 0$, $H_m/H = 0.1$, $R_m/a = 0.15$.

2.3. *Outline of numerical experiments*

The experiments are designed to study: (i) the effect of the mountain on the structure and trajectory of the dipole, and (ii) the long-term motions generated over the topography. The relevant time scale is the rotation period of the system, $T = 4\pi/f_0$, which defines one 'day'. The time step is a small fraction of one day, $\mathrm{d}t = 0.0239T$. The duration of the simulations was 71.62 days (3000 time steps). The interaction of the dipole with the mountain occurs during the first 15 to 20 days, while the long-lived, residual structures are observed during the subsequent 40 to 50 days.

A total of 27 simulations were performed, as indicated in table 1. The horizontal length scales are given in terms of the vortex radius a, and the vertical ones are compared with the total depth H. The experiments are identified with the nomenclature A_{ij}, B_{ij}, C_{ij}. Characters A, B, C define the type of collision according to three different values of y_0/a. Subscript $i = 1, 2, 3$ indicates three values of the mountain height H_m/H. Subscript $j = 1, 2, 3$ corresponds to three mountain radii R_m/a. For instance, the case shown in figure 1 corresponds to experiment B_{22}: a 'northern' collision against a mountain with medium height and medium width ($y_0/a = 1$, $H_m/H = 0.3$, $R_m/a = 2$). All simulations were performed within a square, closed box of side $L \times L$ with $L = 20a$. Note that the domain size is several times larger than the size of the dipole and the horizontal scale of the mountain, $L \gg a, R_m$. The vortex is initially located in the x-direction at $x_0 = -L/3 = -6.667a$. Because the dipole moves initially towards the centre of the domain, the vortex-mountain interaction takes place far from the (no-slip) lateral walls.

The speed of the dipole is almost one vortex radius per day, $U = 0.84a/T$. Thus, from (2.8) the energy is $E_0 = 4.43Ha^4/T^2$. From (2.9), the absolute-value circulation in each of the parts is $\Gamma_0 = 5.74a^2/T$. The viscous coefficient is set to obtain a Reynolds number of $Re = Ua/\nu = 1500$, while the Rossby number is $Ro = U/f_0a = 0.067$. Thus, the initial vortex resembles a nearly inviscid, slowly moving vortex. These numbers are attainable in laboratory experiments in a rotating table, while being sufficiently adequate to explore the dynamics of geophysical cases. For instance, typical values of experimental dipoles in a rotating tank with tap water are $f_0 = 1\ \mathrm{s}^{-1}$, $\nu = 10^{-6}\ \mathrm{m}^2\ \mathrm{s}^{-1}$, $a = 0.15$ m, $U = 0.01\ \mathrm{ms}^{-1}$ (Zavala Sansón *et al.* 2001; Tenreiro *et al.* 2006). Maximum depths H in different experimental arrangements range between 0.2 and 1 m (Zavala Sansón & van Heijst 2014).

2.4. *Numerical method*

The numerical scheme is a finite differences code that has been used in several previous works of experimental rotating flows over topography (Zavala Sansón & van Heijst 2014). The code was originally developed by R. Verzicco and P. Orlandi for two-dimensional flows (Orlandi 1990) and later extended to include rotation effects by J. van Geffen. Further modifications were included by Zavala Sansón & van Heijst (2002) to account for

variable topography effects and Ekman friction. For a homogeneous fluid, the code solves the vorticity equation (2.3) to obtain the vertically uniform vorticity ω. The governing equations are solved in a rectangular grid, in which an Arakawa scheme is used to discretise the nonlinear terms, thus avoiding spurious production of energy (Verzicco *et al.* 1995). The viscous terms are discretised with a centred, second-order scheme that reduces numerical diffusion. Time advancement is performed with an explicit, third-order Runge–Kutta method.

We used a grid of 257×257 points, which was sufficient to resolve the vorticity field very well. To improve the results even further, we used a finer grid with 513×513 points and a time step of $0.008T$. Using this later grid, we checked that the influence of the lateral walls is negligible by repeating the simulations with a larger domain ($L = 40a$). We also verified that the main results hold at higher Reynolds number $O(10^4)$; however, some spurious wiggles appear in the vorticity field, so we report only the $O(10^3)$ Reynolds number simulations.

3. Encounter of dipoles with mountains

Our first task is to analyse the vortex structure and trajectory when encountering the mountain. In this section, we describe two types of flow scenarios with different qualitative characteristics which will be referred to as weak and strong interactions.

3.1. *Weak interactions*

Weak interactions consist of the initial dipole passing over the topography with a deflected trajectory towards its right-hand side, that is, towards the anticyclonic side. Then, the dipole moves away from the mountain, maintaining a coherent structure. To illustrate this behaviour, figure 2 shows three examples of the frontal collision with the low mountain and different radius (experiments A_{11}, A_{12}, A_{13}). The dynamics of this phenomenon is elementary: as the dipole approaches and climbs the topography, the anticyclonic part becomes stronger because fluid columns are squeezed while the cyclonic part becomes weaker. As a result, the dipole trajectory is deflected to the right (looking in the direction of propagation). As the vortex moves downhill, it recovers its symmetric structure approximately.

The modification of the trajectory depends on the height of the topography because of the squeezing effects. Additionally, the mountain width is relevant because the dipole becomes asymmetric during a more extended time-lapse for a greater radius (as observed in figure 2*c*). Weak interactions are also found in experiments $(ABC)_{23}$ and C_{33} (not shown). Thus, the change of trajectory depends not only on the mountain parameters but also the initial y-position of the dipole.

3.2. *Strong interactions*

Strong interactions occur when the structure of the colliding dipole is sensibly modified. Figure 3 presents three examples with different y_0 and a narrow mountain with medium height (experiments A_{21}, B_{21}, C_{21}). As the dipole climbs the mountain, some fluid initially located on the summit is dragged downhill generating a new patch of positive relative vorticity (owing to stretching effects). This newly formed vortex pairs the original anticyclone and both structures conform a modified dipole that moves away from the topography. The new cyclone is formed during strong interactions because stretching effects are enhanced when the mountain is higher (in comparison with lower

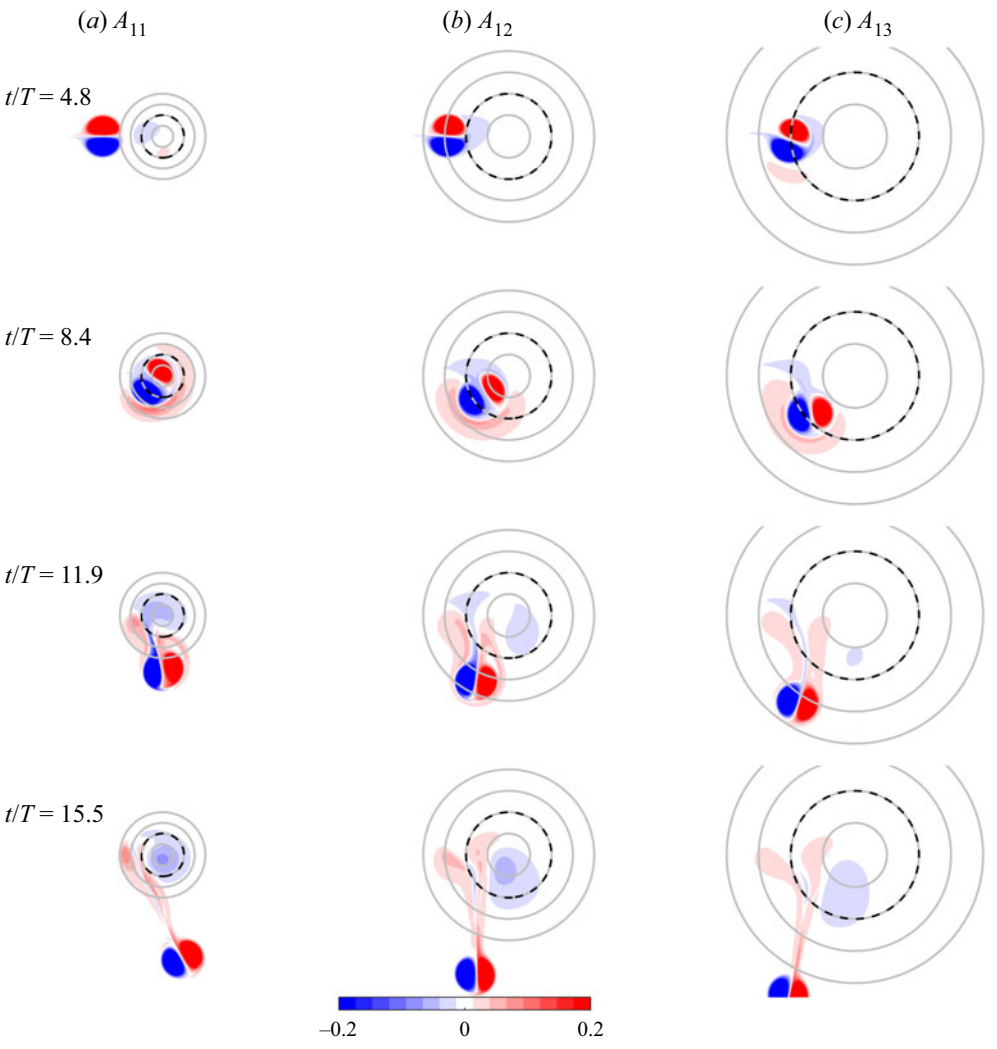

Figure 2. Relative vorticity distributions (ω/f_0) showing weak interactions at times $t/T = 4.8$, 8.4, 11.9 and 15.5 ($T = 4\pi/f_0$) in experiments A_{1j}: $y_0 = 0$, $H_m/H = 0.1$ and (*a*) $R_m/a = 1$, (*b*) $R_m/a = 2$ and (*c*) $R_m/a = 3$. Topography contours as explained in figure 1. The domain shown is a $12a \times 10a$ rectangle (so the lateral walls are not visible).

topographies, as shown in figure 2). The resulting dipole has a more irregular shape and trajectory that is difficult to predict. For instance, the emerging dipole in figure 3(*b*) is retroflected.

Because the vortex–mountain collision is nearly inviscid (which will be shown quantitatively in § 4), the quasi-conservation of potential vorticity (PV) illustrates the material exchange of fluid during strong interactions. Figure 4 presents the PV fields of the same examples shown in figure 3. Indeed, the PV plots reveal that the negative part of the original dipole is always expelled from the mountain when pairing with the fluid descending from the topography. The PV evolution indicates that the remaining motions over the mountain do not contain fluid from the anticyclonic part of the dipole.

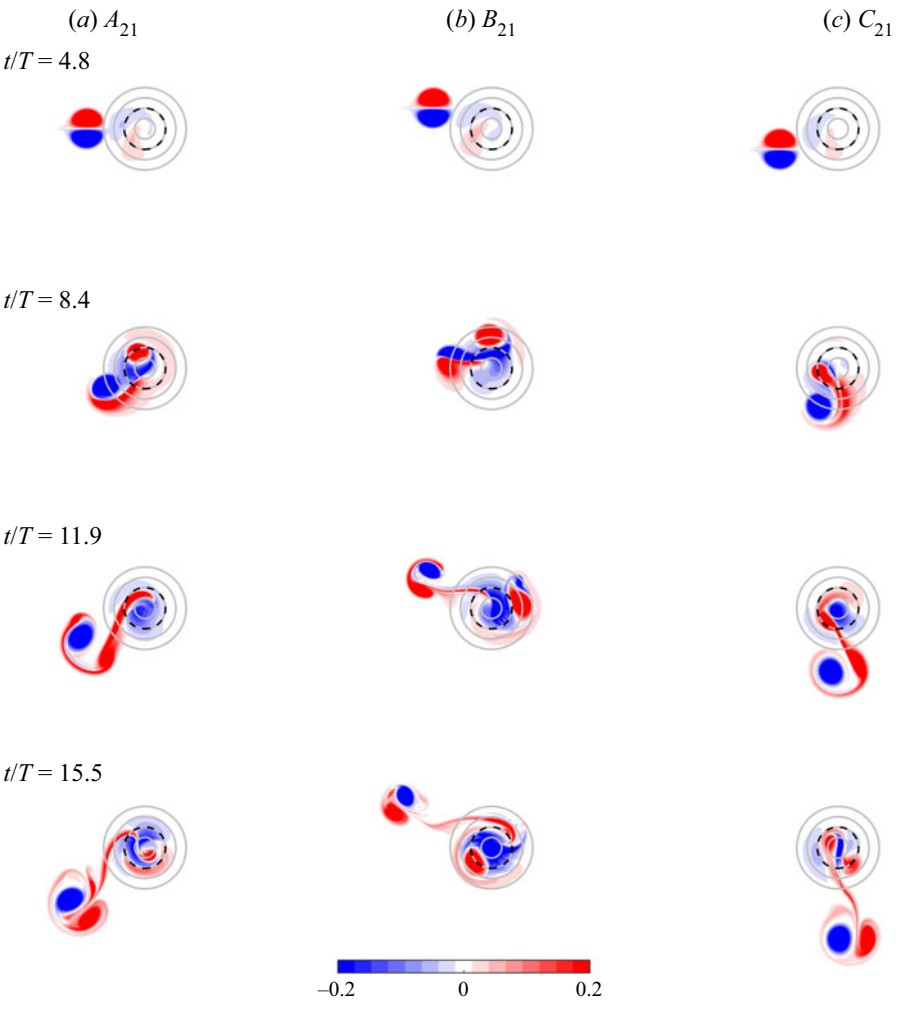

Figure 3. Relative vorticity distributions (ω/f_0) showing strong interactions in experiments ABC_{21}: $H_m/H = 0.3$, $R_m/a = 1$ and (*a*) $y_0 = 0$, (*b*) $y_0/a = 1$ and (*c*) $y_0/a = -1$. Topography contours as in figure 1.

A summary of the resulting interaction, weak or strong, is shown in the following matrix arrangement:

$$\begin{pmatrix} (ABC)_{11} : \textit{Weak} & (ABC)_{12} : \textit{Weak} & (ABC)_{13} : \textit{Weak} \\ (ABC)_{21} : \textit{Strong} & (ABC)_{22} : \textit{Strong} & (ABC)_{23} : \textit{Weak} \\ (ABC)_{31} : \textit{Strong} & (ABC)_{32} : \textit{Strong} & \begin{matrix}(AB)_{33} : \textit{Strong} \\ C_{33} : \textit{Weak}\end{matrix} \end{pmatrix}. \tag{3.1}$$

3.3. *Point-vortices modulated by topography*

The dynamical mechanisms of weak and strong interactions are inviscid, as we discuss now with a point-vortex model. The strength of point vortices is modulated by local topography according to the conservation of volume and potential vorticity (van Heijst 1994).

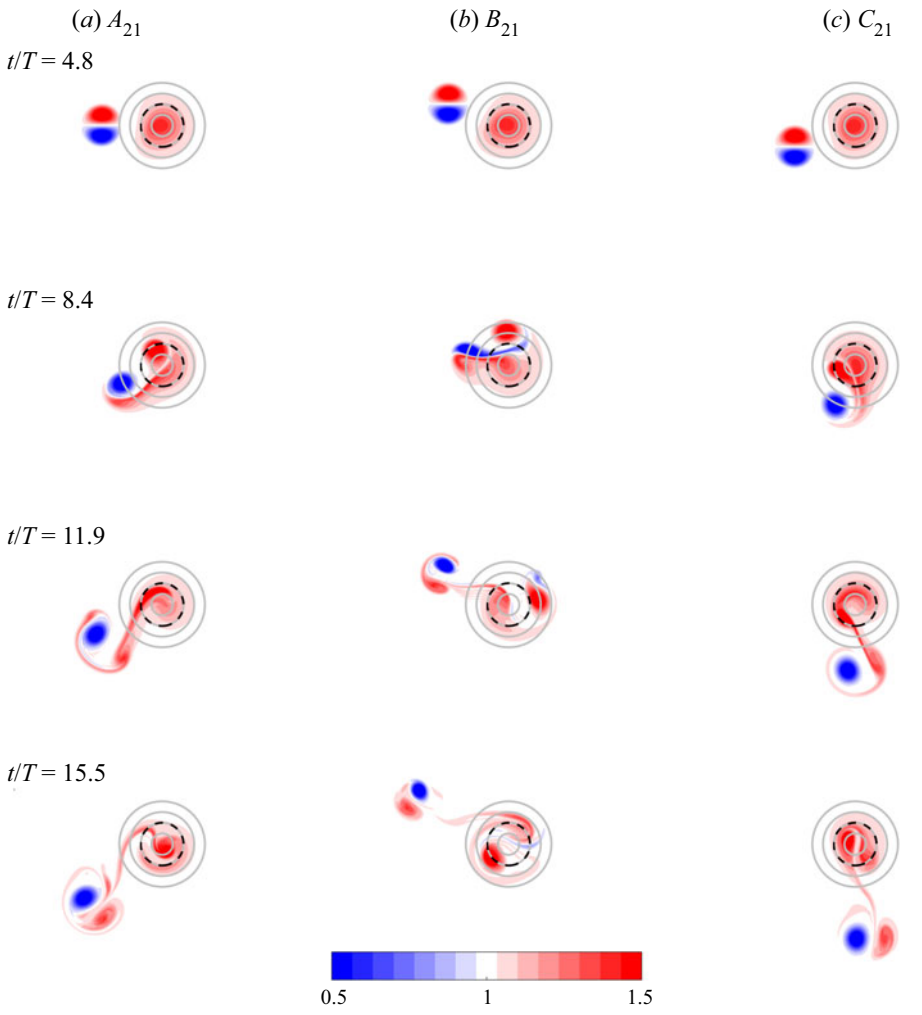

Figure 4. Potential vorticity distributions (qH/f_0) in the strong interactions shown in figure 3. Note that $qH/f_0 = 1$ (white colour) corresponds to fluid with no relative vorticity and away from the mountain.

The strength of a point vortex is defined as the circulation $\Gamma = \zeta A$, where ζ is the vorticity averaged over a cross-sectional area A of the columnar vortex with depth h. The value of these functions depend on the vortex position $x(t)$, $y(t)$ at time t. The volume and potential vorticity conservation are given by

$$A(x, y)h(x, y) = A_0 h_0, \quad \frac{f_0 + \zeta(x, y)}{h(x, y)} = \frac{f_0 + \zeta_0}{h_0}, \tag{3.2a,b}$$

where ζ_0, h_0 and A_0 indicate initial values. Combining these expressions shows that the circulation is modified as the vortices transit from deep to shallow regions or vice-versa, according to the formula

$$\Gamma(x, y) = \Gamma_0 + f_0 A_0 \left(1 - \frac{h_0}{h(x, y)}\right). \tag{3.3}$$

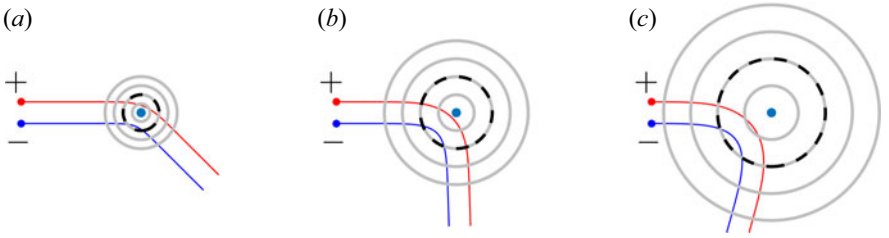

Figure 5. Trajectories of two oppositely signed point vortices representing weak interactions with a low mountain of height $H_m/H = 0.1$ and radius: (*a*) $R_m/a = 1$, (*b*) $R_m/a = 2$, (*c*) $R_m/a = 3$. The vortices are denoted with +, − signs and the initial positions are $(-6.667, 0.6)a$ and $(-6.667, -0.6)a$, respectively (frontal collision). The initial circulations are $\pm\Gamma_0 = \pm 5.74a^2/T$ and the reference areas are chosen as $A_0 = 0.54\pi a^2$. The experiments are equivalent to simulations A_{11}, A_{12} and A_{13}, shown in figure 2.

The motion of a point vortex is induced by the presence of its neighbours. Given the initial positions and strengths of n vortices, the new positions are calculated with $2n$ ordinary differential equations

$$\frac{\mathrm{d}x_k}{\mathrm{d}t} = -\frac{1}{2\pi}\sum_{l\neq k}\Gamma_l(x_l, y_l)\frac{(y_k - y_l)}{d_{kl}^2}, \quad \frac{\mathrm{d}y_k}{\mathrm{d}t} = \frac{1}{2\pi}\sum_{l\neq k}\Gamma_l(x_l, y_l)\frac{(x_k - x_l)}{d_{kl}^2}, \qquad (3.4a,b)$$

where d_{kl} is the separation between vortices k and l. Given the spatially dependent strength of the vortices (3.3), the positions (3.4*a*,*b*) are easily calculated with the Matlab solver ode45, based on an explicit Runge–Kutta scheme. The model was applied by Tenreiro *et al.* (2006) to study the deflection of dipole trajectories passing over a topographic step. In the absence of topography, modulated vortices were first used by Kono and Yamagata (cited by van Heijst 1994) and Zabusky & McWilliams (1982).

Weak interactions are modelled using two oppositely signed point-vortices with initial strengths $\pm\Gamma_0$ separated by a distance d_{12}. The circulation Γ_0 is chosen as in the simulations (§ 2.3) and $d_{12} = 1.2a$. The dipole starts sufficiently far from the mountain, so the initial depth is $h_0/H = 1$. Figure 5 shows three examples of frontal encounters of dipolar vortices against low mountains. The trajectories can be compared with the results obtained for experiments A_{1j} shown in figure 2. As the vortices climb the topography, the ratio $H/h(x, y)$ becomes greater than one because the fluid depth over the mountain is smaller than the initial depth. The negative part of the dipole becomes stronger than the positive part according to (3.3):

$$\left.\begin{array}{ccc} \text{Cyclone strength} & & \text{Anticyclone strength} \\ \Gamma_0 + f_0 A_0\left(1 - \dfrac{H}{h(x,y)}\right) & < & -\Gamma_0 + f_0 A_0\left(1 - \dfrac{H}{h(x,y)}\right). \end{array}\right\} \qquad (3.5)$$

Thus, the dipole trajectory is deflected to the right, that is, towards the stronger part. The deflection is more significant for larger mountain radius, a result that was also observed in the simulations. The reason is that the time that the dipole remains asymmetric over the topography is longer for a larger mountain radius (as in figure 5*c*). As the dipole moves downhill, it recovers its linear motion.

Strong interactions can be mimicked with a suitable arrangement of three modulated point vortices: the original symmetrical dipole and a new vortex with initial strength $\Gamma_{03} = 0$ located near the summit at depth $h_{03} < H$. The additional vortex will be displaced

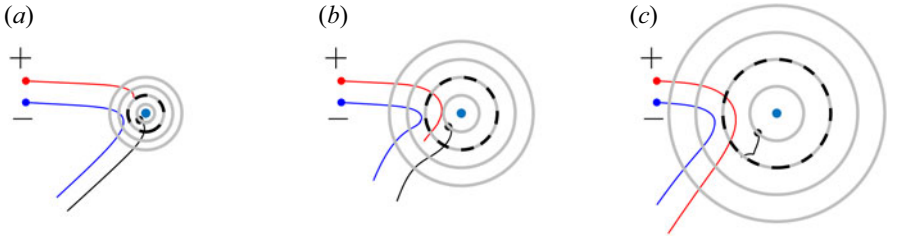

Figure 6. Trajectories of three point-vortices representing strong interactions with a submarine mountain of height $H_m/H = 0.3$ and radius: (*a*) $R_m/a = 1$, (*b*) $R_m/a = 2$, (*c*) $R_m/a = 3$. The vortices forming the dipole are identical to those in figure 5 but now initially located at $(-6.667, 1.8)a$ and $(-6.667, 0.6)a$ ('northern' collision). Initially, the strength of the third vortex is $\Gamma_{03} = 0$, it is located at $(-R_m, -R_m)$ and its subsequent trajectory is denoted with a grey curve. The experiments are equivalent to simulations B_{21}, B_{22} and B_{23}.

downhill by the arriving dipole and, according to (3.3), it will acquire a strength

$$\Gamma_3(x, y) = f_0 A_{03} \left(1 - \frac{h_{03}}{h(x, y)}\right). \tag{3.6}$$

The reference area is chosen as $A_{03} = \Gamma_0/[f_0(1 - h_{03}/H)]$, so $\Gamma_3 = \Gamma_0 > 0$ when displaced downhill (i.e. when $h(x, y) \to H$). This example aims to show that the third vortex may be captured by the anticyclonic part of the original dipole, thus forming a new dipolar structure moving away from the topography.

Figure 6 shows three examples of a 'northern' collision over medium height mountains $H_m/H = 0.3$ with different radius (as those in simulations B_{2j}). The third vortex over the mountain is initially located slightly off the summit. In figure 6(*a*,*b*), the dipole approaches the mountain and displaces the third vortex downhill, which then acquires positive relative vorticity. Then, such a vortex pairs with the anticyclonic part of the original dipole and together move away from the topography. The original cyclone remains static over the mountain as the newly formed dipole separates from it. In contrast, for the wide mountain (figure 6*c*) the interaction is weak again: the original dipole simply deviates to the right.

The representation of strong interactions with three-point vortices may fail when using slightly different values in the initial position of the third vortex over the hill. This problem is to be expected because the evolution of three-point vortices is, in general, very sensitive to the initial conditions (see Aref 1979, 2009 and references therein). Nevertheless, the dynamical mechanism is well-illustrated by choosing suitable values.

4. Residual flow over the mountain

Our second task is to study the residual flow over the mountain. Residual motions are defined as flow structures persisting for long times after the fluid over the summit has been perturbed (in this study, by the passing of the original dipole).

4.1. *Residual energy*

A quantitative signature of residual motions is the time evolution of the kinetic energy over the mountain before and after the passing of the original dipole. The amount of energy per density over the mountain is defined for a circle with radius $2R_m$ centred at the mountain as

$$E_m(t) = \frac{1}{2} \iint [u(x, y, t)^2 + v(x, y, t)^2] h(x, y)\, \mathrm{d}x\, \mathrm{d}y, \quad \sqrt{x^2 + y^2} \leqslant 2R_m. \tag{4.1a,b}$$

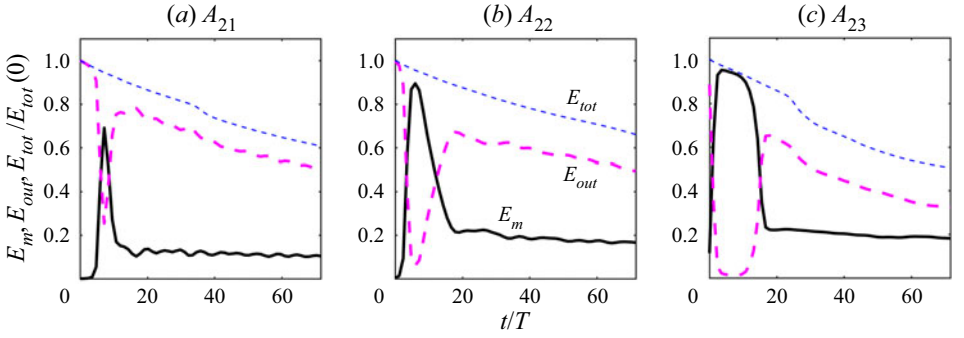

Figure 7. Time evolution of the kinetic energy over the mountain E_m (solid lines), outside the mountain E_{out} (thick dashed lines) and the total energy $E_{tot} = E_m + E_{out}$ (thin dashed lines) in experiments A_{2j} (where $H_m/H = 0.3$) with (*a*) $R_m/a = 1$, (*b*) $R_m/a = 2$, (*c*) $R_m/a = 3$. All values are normalised with the energy of the initial dipole $E_{tot}(0) = E_0$.

The exterior energy $E_{out}(t)$ is calculated with the same expression but integrating outside the circle. The total energy is $E_{tot}(t) = E_m(t) + E_{out}(t)$.

For instance, figure 7 shows the time evolution of E_m, E_{out} and E_{tot} in experiments A_{2j} (frontal collision with a medium height mountain and different radii). At early times the energy over the mountain is zero and then increases abruptly as the original dipole passes over. Afterwards, E_m decreases and reaches a value that remains nearly stationary during the rest of the simulations. The energy of the long-lived residual flow persists for approximately 50 days. The energy at the outer region E_{out} is mainly associated with the original dipole and decays continuously far away from the mountain owing to viscous effects.

In 25 of the 27 experiments, the residual energy fluctuated between 5 and 25 % of the initial total energy and was lower than the outer value, $E_m < E_{out}$. Only in two strong interactions did the energy over the mountain slightly surpass the external energy (simulations B_{21} and B_{31}, which shall be examined below). Indeed, residual motions are not necessarily weak: the strength will depend on the details of the perturbation from which they are generated. The type of flow, in turn, will depend on the height and width of the mountain, as we discuss next.

4.2. *Motion classes*

The long-lived structures over the summit can be classified according to the qualitative features of the vorticity fields during extended periods. A common feature of all residual motions is that they rotate clockwise around the topography. The sense of this rotation is associated with the direction of propagation of topographic Rossby waves, which travel with shallow water to the right in the Northern Hemisphere. In the following descriptions, we focus on the residual flows over the mountain, recalling that the original dipole has moved away and it is no longer visible.

4.2.1. *Asymmetric dipoles*

The most conspicuous residual motions over the topography are asymmetric dipolar structures, in which the anticyclonic side is concentrated near the summit, while the cyclonic part spreads more at the periphery. These vortices are mostly generated during strong interactions over narrow mountains ($R_m/a = 1$). Furthermore, the newly formed

structures rotate clockwise as a whole (with shallow water to the right). A residual dipolar vortex is made of the cyclonic part of the original dipole and the negative vorticity generated over the summit. After a brief adjustment period, the asymmetric dipole over the mountain is well-established, which thereafter persists for long times.

Figure 8 shows three examples of residual dipoles generated during experiments B_{i1} (northern collision with low, medium and tall mountains with short radius). The vorticity fields in each column correspond to four snapshots at late times in the simulations. As expected, the residual dipoles are more intense for steeper mountains (panels (*b*) and (*c*)) because their origin arises from stretching effects. The whole dipolar structures rotate clockwise at different angular speeds $-\Omega$ (with $\Omega > 0$), as can be directly inferred because the time difference between each plot is the same. To obtain Ω, we measured the orientation angle φ of the dipoles during a time span in which the structures are clearly identified. Figure 9 shows that in such periods the dipoles rotate almost two (B_{11}), seven (B_{21}) and ten (B_{31}) times around the respective mountain. The linear relationship $\varphi \sim -\Omega t$ shows that the angular speed is indeed approximately constant in the three cases. Furthermore, Ω is faster for higher mountains (numerical values are shown in the figure caption). The formation and evolution of the residual dipole in simulation B_{21} are shown in the supplementary movie 1 available at https://doi.org/10.1017/jfm.2021.567.

The residual dipoles remain coherent over long periods, which is an indication that they are stable features. Such persistence occurs regardless of the dipole strength. To support this assertion, consider the positive and negative circulations over the mountain defined as

$$\Gamma_m^{\pm}(t) = \int \omega^{\pm}(x, y, t)\, \mathrm{d}x\, \mathrm{d}y, \quad \sqrt{x^2 + y^2} \leqslant 2R_m, \tag{4.2a,b}$$

where ω^+ and ω^- are the positive and negative values of the vorticity inside the circle of radius $2R_m$, respectively. Of course, the initial circulations inside this region are zero in all of the experiments, $\Gamma_m^+(0) = \Gamma_m^-(0) = 0$.

For instance, figure 10 shows the evolution of $\Gamma_m^{\pm}(t)$ in the simulations presented in figures 8 and 9. As the original dipole perturbs the flow over the mountain during the first ten days, there is an abrupt increase of both curves. After reaching a peak value, the circulations diminish and reach stable values while slowly decaying. Residual values correspond to times after 20–30 days (the plots indicate averages over the last 40 days in each simulation). In these examples, the negative circulation is somewhat stronger than the positive circulation, but there are other experiments in which the contrary occurs. Figure 10(*a*) shows the mountain circulations corresponding to the weak residual dipole discussed in figure 8(*a*). Although rather slow, the resulting dipole and its clockwise rotation remain detectable during the rest of the simulation. In contrast, the long-term circulations in figure 10(*b*,*c*) are higher, which reflects that the residual dipoles are rather intense (see figure 8*b*,*c*). Recall that the latter cases correspond to strong interactions. Either way, residual dipoles maintain a very coherent structure during long periods (several days).

4.2.2. *Convoluted patterns and shielded vortices*

The second class of residual motions consists of a convoluted pattern of positive and negative vorticity patches generated over wide mountains ($R_m/a = 2$ and 3). The structures rotate clockwise. The convoluted patterns result from the generation of dispersive topographic Rossby waves over the mountain slope, which travel with shallow water to the right. Figure 11 presents an example for the wide mountain with radius $R_m/a = 3$ and height $H_m/H = 0.3$ (simulation A_{23}). The process starts at early stages

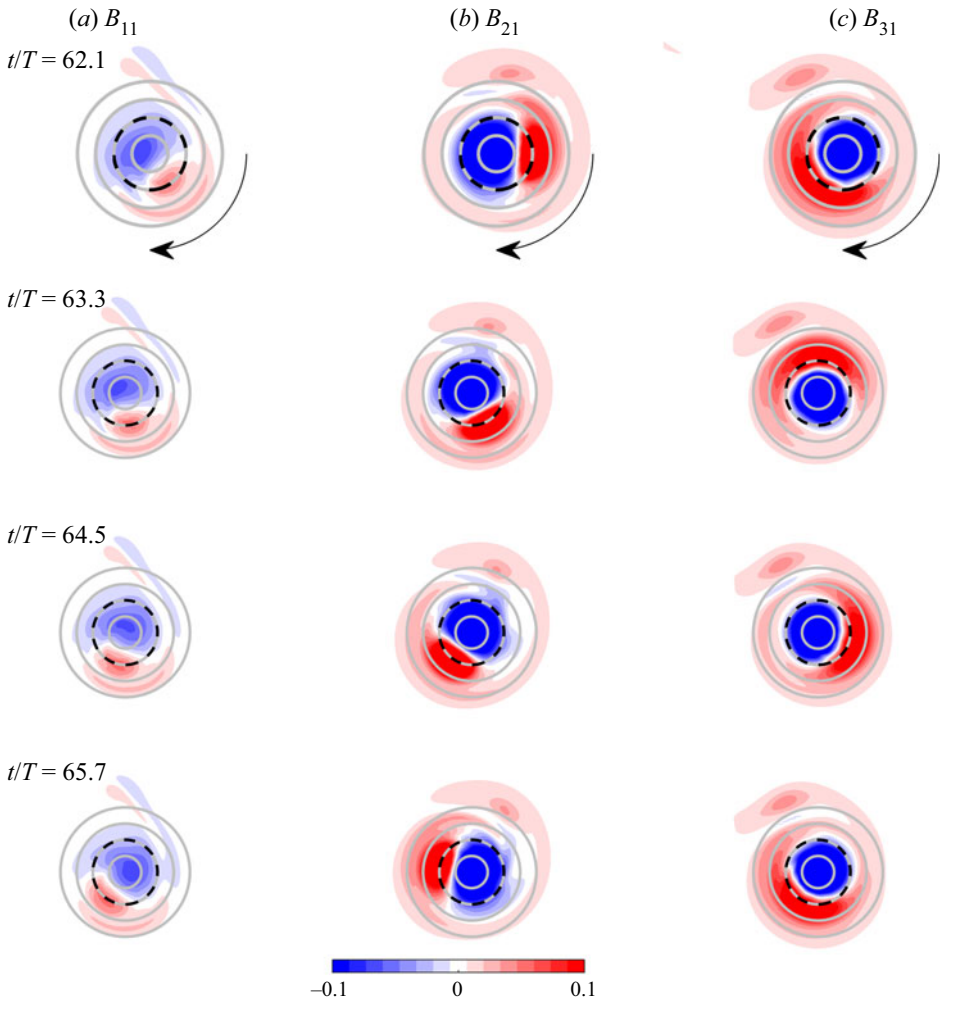

Figure 8. Vorticity distributions showing newly formed dipolar structures over the summit at long times in experiments with $R_m/a = 1$ and (*a*) $H_m/H = 0.1$, (*b*) $H_m/H = 0.3$ and (*c*) $H_m/H = 0.5$. Topography contours as in figure 1. Black arrows indicate the clockwise rotation of the structures.

as the original dipole collides with the mountain at $t/T = 2.4$. The waves manifest as an alternate pattern of positive and negative vorticity patches, which travel clockwise around the summit. The original dipole is deflected downward and moves away from the topography ($t/T = 19.1$). During the rest of the simulation, the waves form the convoluted flow as they continue travelling at different wave speeds around the mountain. The resulting pattern after several weeks ($t/T = 71.6$) is shown in panel (*b*). The whole process is shown in the supplementary movie 2.

In some simulations, the residual flow consisted of an anticyclonic core almost centred over the summit and surrounded by an annulus of positive vorticity. Such structure is observed in simulation A_{31} for a narrow topography (figure 12*a*): an anticyclonic vortex is established over the summit, surrounded by a slightly asymmetric ring of positive vorticity. As in previous cases, the structure rotates clockwise. Over a wider mountain, the

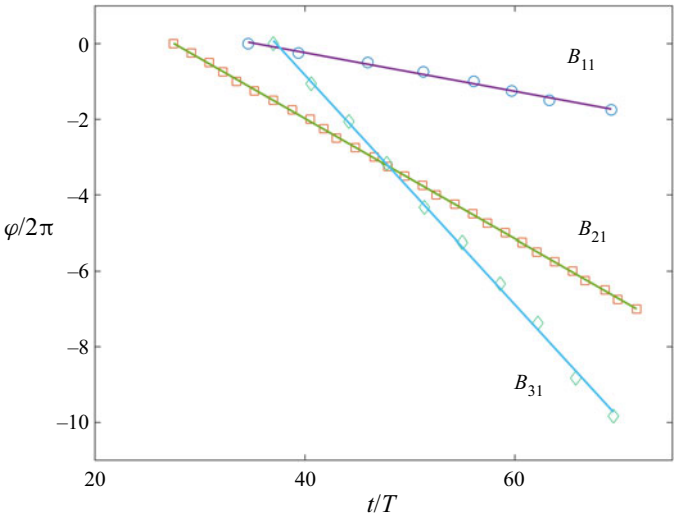

Figure 9. Orientation angle $\varphi/2\pi$ (revolutions) of the residual dipole in experiments B_{i1} (shown in figure 8). Straight lines are the best fit to the data points, where the slope is the angular speed $-\Omega$ in rad/day. Here, B_{11} (circles), $\Omega = 0.32/T$; B_{21} (squares), $\Omega = 1/T$; B_{31} (diamonds), $\Omega = 1.9/T$.

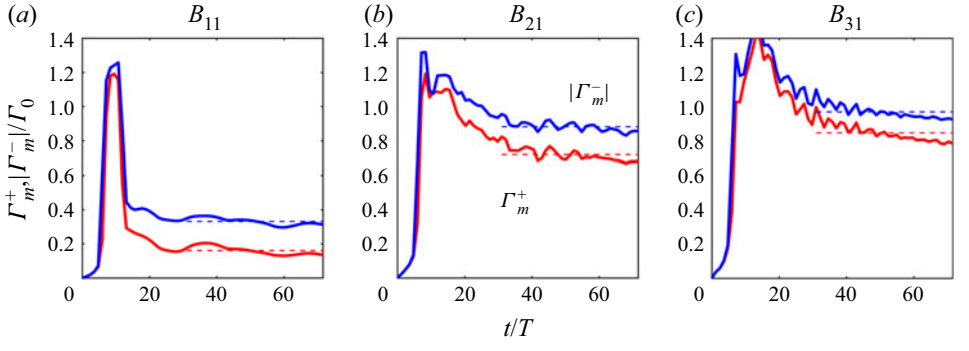

Figure 10. Time evolution of the positive (red lines) and negative (blue lines) circulations over the mountain in experiments B_{i1} (shown in figure 8). The negative circulation is shown as an absolute value. The curves are normalised with the circulation of the initial condition, Γ_0. The average values over the last 40 days $(\langle\Gamma_m^+\rangle, \langle\Gamma_m^-\rangle)/\Gamma_0$ are: (*a*) (0.16, −0.33); (*b*) (0.72, −0.88); (*c*) (0.85, −0.97); these are indicated as absolute values by the horizontal dashed lines.

surrounding cyclonic vorticity may have multiple local maxima, as shown in figure 12(*b*) for experiment A_{22}. Again, the whole structure rotates with shallow water to the right.

4.3. *Quasi-geostrophic analytical solutions of asymmetric dipoles*

Residual vortices are compatible with analytical solutions of barotropic flows over topography. Here we compare the asymmetric dipolar structures over the mountain, discussed in § 4.2.1, with nonlinear QG solutions recently derived by Gonzalez & Zavala Sansón (2021). The derivation is relatively simple but not trivial, so further details should be consulted in that paper. The solutions satisfy the inviscid QG vorticity equation in polar

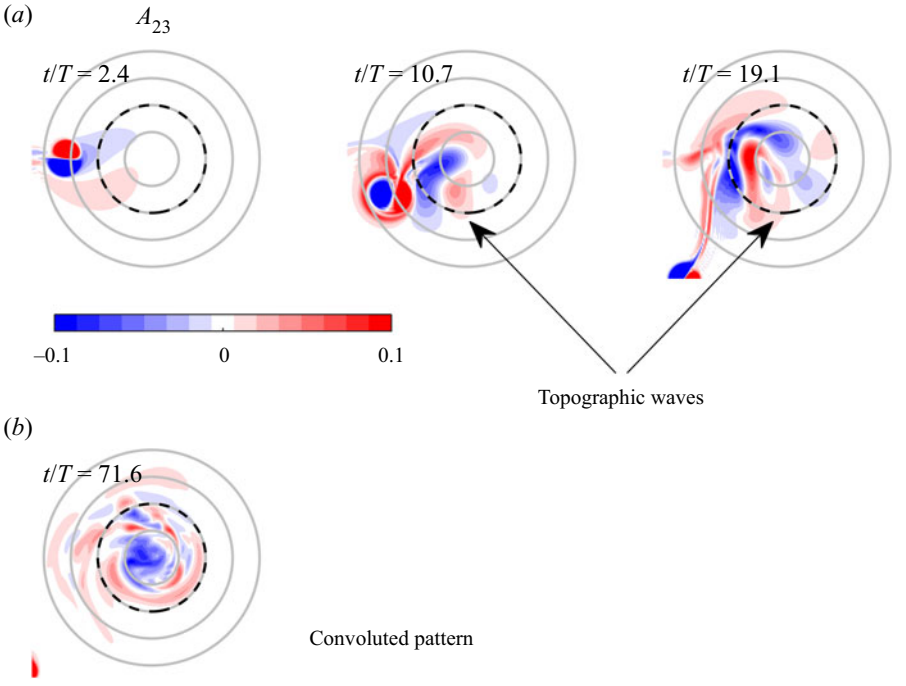

Figure 11. Vorticity distributions (ω/f_0) showing the development of convoluted patterns over the summit at long times in simulation A_{23} ($H_m/H = 0.3$ $R_m/a = 3$): (*a*) the generation of topographic Rossby waves at early times; (*b*) the clockwise-rotating, convoluted pattern at the end of the simulation. Topography contours as in figure 1.

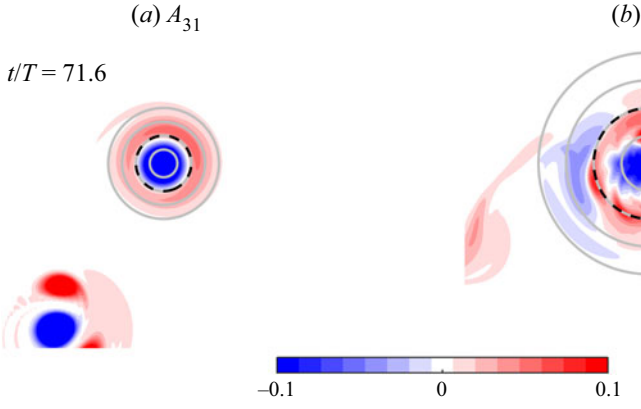

Figure 12. Vorticity distributions (ω/f_0) at time $t/T = 71.6$ in simulations (*a*) A_{31} ($H_m/H = 0.5$ $R_m/a = 1$) and (*b*) A_{22} ($H_m/H = 0.3$ $R_m/a = 2$). The residual flows consist of an anticyclonic vortex shielded by an annulus of positive vorticity. Topography contours as in figure 1.

coordinates (r, θ):

$$\frac{\partial}{\partial t}(\nabla^2\psi_q) + J[\psi_q, \nabla^2\psi_q + \omega_a(r)] = 0, \tag{4.3}$$

where $\psi_q(r, \theta, t)$ is the QG stream function, and J, ∇^2 are the polar Jacobian and Laplacian operators, respectively. The ambient vorticity arising from the presence of the

axisymmetric mountain is

$$\omega_a(r) = \frac{f_0 b(r)}{H}, \tag{4.4}$$

where $b(r) = H_m \exp(-r^2/R_m^2)$ is the same topography used in the simulations. Gonzalez & Zavala Sansón (2021) denoted the ambient vorticity with symbol h, as customary; here we shall use ω_a to avoid confusion with the fluid depth $h(r) = H - b(r)$. The main difference with the SW system is that in QG theory the mountain height is restricted to small values, $H_m \ll H$ (Carnevale *et al.* 1995). Further, the relative vorticity is simply $\nabla^2\psi_q$, instead of the more elaborate expression (2.2) in the SW model. Note that the stream function ψ_q is defined with the opposite sign of the transport function ψ. The QG potential vorticity is $\nabla^2\psi_q + \omega_a(r)$.

The vortical solutions are based on azimuthal modes $m = 0$ (circular monopoles) and $m = 1$ (asymmetric dipoles) over an isolated topographic feature, such as the Gaussian mountain used here. In Appendix A we discuss how to construct the relative vorticity field for dipolar modes. Given H and f_0, the dipolar solutions depend on four additional parameters: the mountain height H_m and its horizontal scale R_m, the amplitude $|\hat{\psi}_1|$, and the factor c_0 (with units of inverse length) with which the radial coordinate is scaled as $s = c_0 r$. The vortex radius is defined as s_l/c_0, where $s_l = 3.8317$ is the first zero of the Bessel function $\mathrm{J}_1(s)$; note the resemblance with the size of the Chaplygin–Lamb dipole (2.7).

A crucial feature of the analytical dipole is that the structure rotates clockwise at a constant angular speed $-\Omega$, which is calculated with (A11). A close inspection of this formula reveals that Ω depends explicitly on H_m and R_m contained in the ambient vorticity $\omega_a(r)$ (see (4.4)), and implicitly on c_0, contained in the scaled coordinate s.

Hereafter we construct analytical dipoles that are similar to the residual flows found in simulations B_{11}, B_{21}, B_{31}, shown in figure 8. The flow parameters and other useful quantities are shown in table 2. To obtain the most relevant numbers, we proceeded as follows:

(a) The mountain height H_m and length scale R_m are chosen as in the simulations. The amplitude H_m defines the peak ambient vorticity $\omega_{a0} = \omega_a(0) = f_0 H_m/H$ (to be used below).

(b) To obtain c_0, we estimate the vortex radius as a fraction $\alpha > 1$ of the mountain length scale: $s_l/c_0 = \alpha R_m$. Then, the scaling factor $c_0 = s_l/(\alpha R_m)$ is chosen to obtain the desired angular speed Ω from (A11).

(c) The vortex amplitude is estimated by considering that the solutions are composed of two main terms: a dipolar mode (A4) of order $|\psi_1|$ and a topographic term (A5) proportional to ω_{a0}/c_0^2. By setting $|\psi_1| = 2\omega_{a0}/c_0^2$ we find that the negative circulations Γ_m^- are almost the same as those found in the simulations (presented in figure 10).

Figure 13 shows the analytical vorticity fields. The initial dipole orientations at $t/T = 0$ are chosen to be similar to the cases shown in figure 8 at $t/T = 62.1$. The time interval between successive plots is also the same (1.2 days). The analytical vortices reproduce the most conspicuous characteristics of the simulated dipoles: (i) the asymmetric shape of the structure, with the cyclonic part embracing the anticyclone, and (ii) the angular speed around the mountain. The resemblance of the dipole asymmetry is only qualitative, while the magnitude of the angular speed is quantitatively the same as in the simulations.

Table 2 also shows the theoretical circulations $\Gamma_q^{\pm}$, which are compared with the average residual circulations over the mountain presented in figure 10. For the negative circulations

Scaled parameters	Symbol	B_{11}	B_{21}	B_{31}
Mountain height	H_m/H	0.1	0.3	0.5
Mountain radius	$c_0 R_m$	2.0	2.2	2.4
Vortex amplitudes	$\lvert\psi_1\rvert/(\omega_{a0}/c_0^2)$	2	2	2
Vortex/mountain ratio	$\alpha = s_l/(c_0 R_m)$	1.90	1.75	1.60
Results				
Angular speed	Ω (rad/day)	0.32/T	1.05/T	1.91/T
Positive circulation	$\Gamma_q^+ / \langle \Gamma_m^+ \rangle$	5.76	3.27	3.85
Negative circulation	$\Gamma_q^- / \langle \Gamma_m^- \rangle$	0.88	0.84	1.06

Table 2. Flow parameters used in the analytical solutions shown in figure 13, which mimic the simulations B_{i1} in figure 8. The magnitude of the angular speed Ω is calculated with (A11). The theoretical circulations Γ_q^+, Γ_q^- are compared with the average residual values calculated in the simulations $\langle \Gamma_m^+ \rangle$, $\langle \Gamma_m^- \rangle$ (see caption of figure 10).

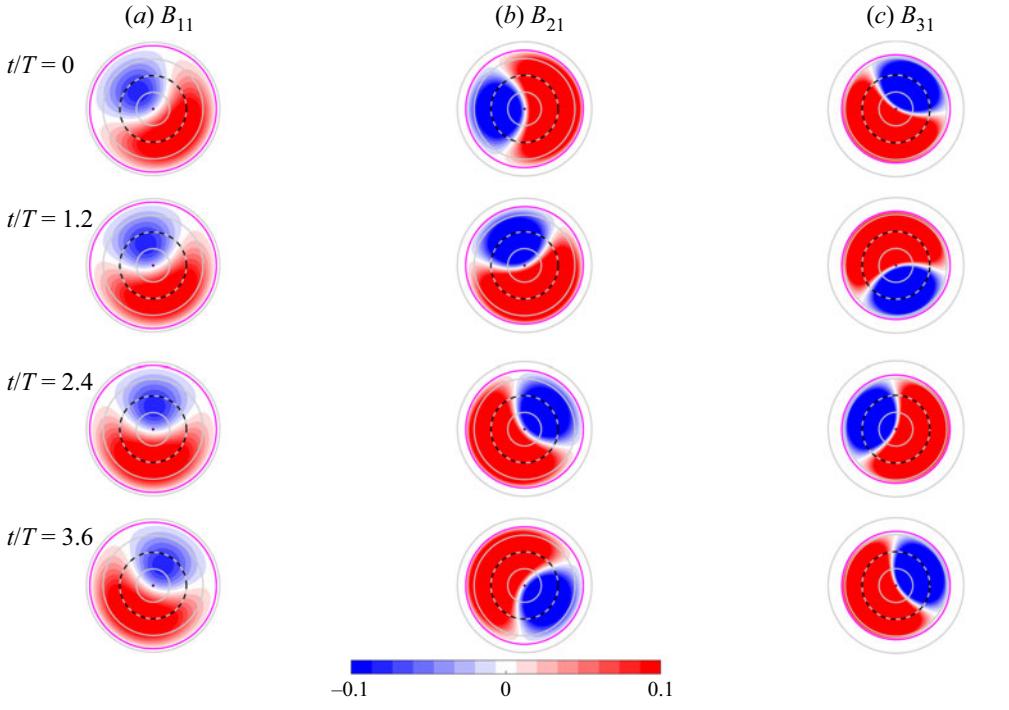

Figure 13. Analytically calculated relative vorticity distributions (ω/f_0) of asymmetric dipolar vortices over the Gaussian mountains used in simulations B_{i1}. The vorticity fields are obtained from (A10), (A4)–(A6) using the parameters in table 2. The magenta circles indicate the size of the interior solution. Topography contours as in figure 1.

there is a good agreement between the theory and the simulations (the relative difference is between 6 and 16 %). However, the positive circulations of the analytical solutions exceed the numerical values by up to 3 to 5 times. A possible reason for this discrepancy may be the absence of dissipation in the inviscid solutions. Additionally, recall that the solutions are QG, in contrast with the SW dynamics resolved in the numerical experiments.

Summarising, the form and behaviour of residual asymmetric dipoles in the SW simulations are consistent with the nonlinear analytical solutions in QG. Some qualitative and quantitative features are remarkably well-reproduced, though some others are not.

5. Summary and discussion

We presented quasi-2-D, SW numerical simulations of barotropic flows over a topographic mountain in a constantly rotating system. The dynamical model assumes a columnar motion over the whole depth, whose relative vorticity is modulated by changes in height as the fluid columns move over the topography. In the first part, we studied the collision of an initially symmetric dipole against the mountain. The main results were further explored with a topographically modulated point-vortex model. Afterwards, we carefully examined the long-term residual flow over the topography. Such a persistent flow (trapped over the mountain) was compared with QG analytical solutions. The main findings are discussed separately.

5.1. *Collision of dipoles against mountains*

The encounter of an initially symmetric dipole with different submerged mountains revealed two dynamical scenarios: weak and strong collisions. In the former case, the dipole structure is only slightly modified while the trajectory is being deflected towards the anticyclonic side. The intensification of the anticyclone arising from squeezing effects clearly explains this behaviour. At later times, the vortex moves away from the topography. Weak collisions mostly occur when the mountain height is sufficiently small.

In contrast, strong collisions occurred over higher mountains. These interactions consisted of the formation of a new cyclonic vortex from stretching effects, which paired with the original anticyclone side of the dipole and together moved away from the mountain. This striking effect has been observed in laboratory experiments with monopoles (Zavala Sansón *et al.* 1999) and dipoles (Tenreiro *et al.* 2006) approaching a step-topography. The problem becomes complicated when using a mountain because of the round shape and steepness of the slope.

Weak and strong interactions are nearly inviscid, as shown by the small decay of the total energy (approximately 10 %) during the occurrence of these processes (first 10–20 days in figure 7). The results obtained with the point-vortex model support the notion that the predominant dynamical mechanisms are inviscid.

The present results may serve as a starting point to study the fate of the colliding dipole in a stratified fluid, as in oceanic cases. It is expected that in the presence of vertical stratification, the surface vortices will experience weaker effects from the bottom topography. To what extent the topographic mountain affects the passing of a travelling vortex in the upper layers? A first model to study such cases might be the equivalent-barotropic dynamics used to simulate atmospheric and (less often) oceanic flows (Killworth 1992; Zavala Sansón 2019). The equivalent-barotropic model considers a flow with a given vertical structure, whose magnitude changes with depth while maintaining the same direction. For instance, a vertical exponential decay implies that the active motion is confined to the upper layer, which inhibits the interaction of a vortex passing over the topography. The implications are relevant to understand better the long-range propagation of mesoscale geophysical vortices in the world oceans. This research line is under current investigation. Another dynamical effect to be taken into account is the β-effect (the constant latitudinal gradient of the Coriolis parameter). The combined effects of topography and β on vortices is usually a complicated matter (van

Geffen & Davies 2000; Zavala Sansón 2002; Herbette, Morel & Arhan 2005) that deserve further study.

5.2. *Long-term residual flows*

A different problem was the residual flow left over the mountain during the subsequent 40 to 50 days. The remaining flow patterns over the mountain are so persistent that they can be regarded as the typical signature of the perturbed flow over the topography. We noticed three types of residual motions. The most notorious structures were long-lived asymmetric dipoles that rotate clockwise as a whole over narrow mountains. Over wide topographies, in contrast, the flow patterns may be highly convoluted. The third type was quasi-circular anticyclones over the mountain, surrounded by an annulus of cyclonic vorticity. All of these motions are mostly inviscid, as revealed from the time evolution of the energy over the mountain (figure 7).

Oceanic flows over a Gaussian mountain were studied numerically by Verron & Le Provost (1985) in a different context. Their f-plane experiments were QG and simulated a permanent, uniform stream passing over the mountain. The authors found the entrapment of an anticyclonic vortex, as well as different transient regimes which were attributed to the generation of topographically trapped waves. In contrast, the present SW simulations allow intense flows and relatively abrupt topographies. Nevertheless, some features of the residual flows may also be associated with topographic (Rossby) waves, which are the most basic oscillations admitted by the dynamics. The following evidence points out this relationship:

(i) The generation of waves is observed in the convoluted pattern over wide topographies, as shown in figure 11. The oscillations consist of successive patches of positive and negative vorticity that develop as the flow is perturbed. The waves travel clockwise with shallow water to the right because $f_0 > 0$ (Rhines 1969). The complicated patterns may be associated with the dispersive nature of the waves.

(ii) Topographic Rossby waves are subinertial oscillations. In our simulations, residual flows indeed rotate clockwise at a low frequency, $|2\Omega| < f_0$. Additionally, the frequency increases for higher mountains, as seen in figure 9 (see also Verron & Le Provost 1985, figure 11).

(iii) The formation of asymmetric dipolar vortices over the summit (as in figure 8) is compatible with the shape of analytically derived wave modes (see Zavala Sansón 2010, figure 3). The waves rotate clockwise with an angular speed that depends on the shape of the mountain and the azimuthal and radial wavenumbers. The resemblance of the vorticity distribution is only qualitative, however, because the waves are azimuthally symmetrical modes.

It must be kept in mind that residual motions in our simulations may not behave precisely as linear waves. The nonlinear origin of residual flows may explain the asymmetry of the persistent dipolar structures seen in figure 8(*b*,*c*). Interestingly, a similar asymmetry is characteristic of the nonlinear dipolar solutions of Gonzalez & Zavala Sansón (2021). We showed that some qualitative and quantitative features of the residual dipoles are congruent with the theoretical solutions. Again, no perfect match is expected with the analytical examples, which are based on the QG dynamics.

Assuming that the described residual flows are the natural response of the flow over a mountain, it remains to investigate to what extent they are found in real physical systems. In rotating tank experiments, asymmetric mountain dipoles may be tough to observe because typical laboratory length scales are often short (a few tens of cm). Such conditions make

it difficult to measure the vorticity field in detail. Furthermore, dissipative effects owing to solid walls and lateral friction limit the duration of the experiments. To our knowledge, the only laboratory evidence of asymmetric dipoles trapped over a mountain was reported in the experiments by Zavala Sansón *et al.* (2012). The experiments were performed in a large rotating tank (the Coriolis platform in Grenoble, France), where the mentioned difficulties were significantly overcome. The finding of asymmetric dipoles in that study was fortuitous because the purpose of the experiments was different. The present results may shed some light on how to design future experiments or field measurements to study residual flows more systematically.

Supplementary movies. Supplementary movies are available at https://doi.org/10.1017/jfm.2021.567.

Funding. J.F.G. is grateful for support from the Consejo Nacional de Ciencia y Tecnología (CONACYT, México) and from the Secretaría de Educación de Bogotá (Colombia).

Declaration of interests. The authors report no conflict of interest.

Author ORCIDs.
Luis Zavala Sansón https://orcid.org/0000-0002-0419-5445;
Jeasson F. Gonzalez https://orcid.org/0000-0003-3691-6443.

Appendix A. Analytical solutions of asymmetric dipoles

Here we present a brief account of the nonlinear, QG vortex solutions on the f-plane with axisymmetric topography (mountains and valleys) obtained by Gonzalez & Zavala Sansón (2021) (referred to as GZS21). The most important features are the following:

(i) The solutions are stationary in a uniformly rotating frame around the origin, such that the rotated azimuthal coordinate is $\theta' = \theta + \Omega t$, where the rotation is clockwise (anticlockwise) for $\Omega > 0$ ($\Omega < 0$). Using a scaled radial coordinate $s = c_0 r$, the stationary vorticity equation (4.3) yields

$$J\left[\psi_q'(s,\theta') + \frac{\Omega}{2c_0^2}s^2,\, \nabla^2\psi_q'(s,\theta') + \omega_a(s)\right] = 0. \tag{A1}$$

(ii) The vortex solutions are defined in two regions: (a) an interior flow within a circular area with non-dimensional radius $s_l = 3.8317$ centred at the origin, and (b) an exterior flow to keep the interior distribution confined over the topography:

$$\psi_q'(s,\theta') = \begin{cases} \psi_{I1}(s,\theta') - \dfrac{\Omega}{2c_0^2}s^2 & s \leqslant s_l \\ \psi_{E1}(s,\theta') & s \geqslant s_l. \end{cases} \tag{A2}$$

Subindex 1 indicates that the solutions correspond to dipolar structures.

(iii) The interior solutions are of the form

$$\psi_{I1}(s,\theta') = \psi_{V1}(s,\theta') + \phi(s). \tag{A3}$$

The first term is the mode-1, 2-D dipolar solution found by Viúdez (2019) in the absence of topography:

$$\psi_{V1}(s,\theta') = |\hat{\psi}_1|\mathrm{J}_1(s)\sin\theta', \tag{A4}$$

where $|\hat{\psi}_1|$ is the amplitude. This case corresponds to a symmetrical dipole initially oriented in the horizontal direction and pointing to the left in a planar system. Viúdez

(2019) discussed more general 2-D solutions based on Bessel functions of arbitrary order, J_m ($m = 0, 1, 2\ldots$). The second term in (A3), $\phi(s)$, contains the influence of the topography:

$$\phi(s) = \frac{\omega_{a0}}{c_0^2} C_1 \mathrm{J}_0(s) + \frac{\pi}{2}\mathrm{Y}_0(s) \int_0^s \Pi(s')\mathrm{J}_0(s')s'\,\mathrm{d}s' - \frac{\pi}{2}\mathrm{J}_0(s) \int_0^s \Pi(s')\mathrm{Y}_0(s')s'\,\mathrm{d}s', \tag{A5}$$

where J_0 and Y_0 are the first- and second-kind Bessel functions of order 0, and the radial function $\Pi(s)$ is

$$\Pi(s) = \frac{\omega_{a0} - \omega_a(s)}{c_0^2}. \tag{A6}$$

Note that $\Pi = 0$ at the origin and also in the absence of topography (i.e. when $\omega_a = 0$). The integration constant C_1 in (A5) is set to guarantee the continuity of the vorticity at the interior–exterior boundary (C_1 is explicitly calculated with formula B6 in GZS21, but is not essential in the present analysis).

(iv) The exterior solution $\psi_{E1}(s, \theta')$ is the sum of a potential flow and a uniform vorticity field proportional to s^2 (Meleshko & van Heijst 1994; Viúdez 2019):

$$\psi_{E1}(s, \theta') = \frac{1}{2}|\hat{\psi}_1|\mathrm{J}_1'(s_l)\left(s - \frac{s_l^2}{s}\right)\sin\theta' + d_0 + d_1 \ln s + d_2 s^2 \quad s \geqslant s_l. \tag{A7}$$

The coefficients d_0, d_1 and d_2 are chosen to satisfy the continuity of the stream function, the azimuthal velocity and the vorticity at s_l (formulae (2.25) and B5 in GZS21).

(v) The relative vorticity field is the Laplacian of (A2):

$$\omega_q'(s, \theta') = \begin{cases} \omega_{I1}(s, \theta') - 2\Omega & s \leqslant s_l \\ -2\Omega & s \geqslant s_l, \end{cases} \tag{A8}$$

where the interior vorticity is ((2.13) in GZS21)

$$\omega_{I1}(s, \theta') = c_0^2\left[-\psi_{V1}(s, \theta') - \phi(s) + \Pi(s)\right]. \tag{A9}$$

(vi) In a reference frame fixed to the f-plane, the non-stationary solution is

$$\omega_q(s, \theta, t) = \begin{cases} \omega_{I1}(s, \theta + \Omega t) & s \leqslant s_l \\ 0 & s \geqslant s_l. \end{cases} \tag{A10}$$

A formula for Ω is obtained by considering that the total circulation of the interior region is zero ((2.35) in GZS21):

$$\Omega = \frac{1}{s_l^2}\int_0^{s_l} \omega_a(s)s\,\mathrm{d}s - \frac{\pi}{2s_l}\mathrm{Y}_1(s_l)\int_0^{s_l}[\omega_{a0} - \omega_a(s)]\mathrm{J}_0(s)s\,\mathrm{d}s, \tag{A11}$$

where Y_1 is the Bessel function of the second kind of order 1. The formula is further discussed and applied in § 4.3.

References

Aref, H. 1979 Motion of three vortices. *Phys. Fluids* **22** (3), 393–400.

Aref, H. 2009 Stability of relative equilibria of three vortices. *Phys. Fluids* **21** (9), 094101.

Beckmann, A. & Mohn, C. 2002 The upper ocean circulation at Great Meteor Seamount. *Ocean Dyn.* **52** (4), 194–204.

Camassa, R., Holm, D.D. & Levermore, C.D. 1997 Long-time shallow-water equations with a varying bottom. *J. Fluid Mech.* **349**, 173–189.

Carnevale, G.F., Kloosterziel, R.C. & van Heijst, G.J.F. 1991 Propagation of barotropic vortices over topography in a rotating tank. *J. Fluid Mech.* **233**, 119–139.

Carnevale, G.F., Purini, R., Orlandi, P. & Cavazza, P. 1995 Barotropic quasi-geostrophic f-plane flow over anisotropic topography. *J. Fluid Mech.* **285**, 329–347.

Cenedese, C. 2002 Laboratory experiments on mesoscale vortices colliding with a seamount. *J. Geophys. Res.: Oceans* **107** (C6), 3053.

Chapman, D.C. & Haidvogel, D.B. 1992 Formation of Taylor caps over a tall isolated seamount in a stratified ocean. *Geophys. Astrophys. Fluid Dyn.* **64** (1–4), 31–65.

Flierl, G.R., Stern, M.E. & Whitehead, J.A. Jr. 1983 The physical significance of modons: laboratory experiments and general integral constraints. *Dyn. Atmos. Oceans* **7** (4), 233–263.

Flór, J.-B. & Eames, I. 2002 Dynamics of monopolar vortices on a topographic beta-plane. *J. Fluid Mech.* **456**, 353–376.

van Geffen, J.H.G.M. & Davies, P.A. 2000 A monopolar vortex encounters an isolated topographic feature on a β-plane. *Dyn. Atmos. Oceans* **32** (1), 1–26.

Genin, A. 2004 Bio-physical coupling in the formation of zooplankton and fish aggregations over abrupt topographies. *J. Mar. Syst.* **50** (1–2), 3–20.

Gonzalez, J.F. & Zavala Sansón, L. 2021 Quasi-geostrophic vortex solutions over isolated topography. *J. Fluid Mech.* **915**, A64.

Grimshaw, R., Tang, Y. & Broutman, D. 1994 The effect of vortex stretching on the evolution of barotropic eddies over a topographic slope. *Geophys. Astrophys. Fluid Dyn.* **76** (1–4), 43–71.

van Heijst, G.J.F. 1994 Topography effects on vortices in a rotating fluid. *Meccanica* **29** (4), 431–451.

van Heijst, G.J.F. & Clercx, H.J.H. 2009 Laboratory modeling of geophysical vortices. *Annu. Rev. Fluid Mech.* **41**, 143–164.

Herbette, S., Morel, Y. & Arhan, M. 2005 Erosion of a surface vortex by a seamount on the β plane. *J. Phys. Oceanogr.* **35** (11), 2012–2030.

Hinds, A.K., Eames, I., Johnson, E.R. & McDonald, N.R. 2009 Laboratory study of vortex dipoles interacting with step topography. *J. Geophys. Res.: Oceans* **114** (C6), C06006.

Hinds, A.K., Johnson, E.R. & McDonald, N.R. 2016 Beach vortices near circular topography. *Phys. Fluids* **28** (10), 106602.

Hopfinger, E.J. & van Heijst, G.J.F. 1993 Vortices in rotating fluids. *Annu. Rev. Fluid Mech.* **25** (1), 241–289.

Hughes, C.W. & Miller, P.I. 2017 Rapid water transport by long-lasting modon eddy pairs in the southern midlatitude oceans. *Geophys. Res. Lett.* **44** (24), 12–375.

Huppert, H.E. & Bryan, K. 1976 Topographically generated eddies. *Deep-Sea Res.* **23**, 655–679.

Killworth, P.D. 1992 An equivalent-barotropic mode in the Fine Resolution Antarctic Model. *J. Phys. Oceanogr.* **22** (11), 1379–1387.

van Leeuwen, P.J. 2007 The propagation mechanism of a vortex on the β plane. *J. Phys. Oceanogr.* **37** (9), 2316–2330.

Meleshko, V.V. & van Heijst, G.J.F. 1994 On Chaplygin's investigations of two-dimensional vortex structures in an inviscid fluid. *J. Fluid Mech.* **272**, 157–182.

Nencioli, F., Dall'Olmo, G. & Quartly, G.D. 2018 Agulhas ring transport efficiency from combined satellite altimetry and Argo profiles. *J. Geophys. Res.: Oceans* **123** (8), 5874–5888.

Nycander, J. & Lacasce, J.H. 2004 Stable and unstable vortices attached to seamounts. *J. Fluid Mech.* **507**, 71–94.

Orlandi, P. 1990 Vortex dipole rebound from a wall. *Phys. Fluids* A **2** (8), 1429–1436.

Pedlosky, J. 1987 *Geophysical Fluid Dynamics*. Springer Science & Business Media.

Rhines, P.B. 1969 Slow oscillations in an ocean of varying depth. Part 2. Islands and seamounts. *J. Fluid Mech.* **37** (1), 191–205.

Ryzhov, E.A. & Koshel, K.V. 2013 Interaction of a monopole vortex with an isolated topographic feature in a three-layer geophysical flow. *Nonlinear Process. Geophys.* **20**, 107–119.

SCHOUTEN, M.W., DE RUIJTER, W.P.M., VAN LEEUWEN, P.J. & LUTJEHARMS, J.R.E. 2000 Translation, decay and splitting of Agulhas rings in the southeastern Atlantic Ocean. *J. Geophys. Res.: Oceans* **105** (C9), 21913–21925.

SUTYRIN, G.G. & GRIMSHAW, R. 2010 The long-time interaction of an eddy with shelf topography. *Ocean Model.* **32** (1–2), 25–35.

TAYLOR, G.I. 1921 Experiments with rotating fluids. *Proc. R. Soc. Lond.* A **100** (703), 114–121.

TENREIRO, M., ZAVALA SANSÓN, L. & VAN HEIJST, G.J.F. 2006 Interaction of dipolar vortices with a step-like topography. *Phys. Fluids* **18** (5), 056603.

TRASVIÑA-CASTRO, A., DE VELASCO GUTIÉRREZ, G., VALLE-LEVINSON, A., GONZALEZ-ARMAS, R., MUHLIA, A. & COSIO, M.A. 2003 Hydrographic observations of the flow in the vicinity of a shallow seamount top in the Gulf of California. *Estuar. Coast. Shelf Sci.* **57** (1–2), 149–162.

VALLIS, G.K. 2017 *Atmospheric and Oceanic Fluid Dynamics*. Cambridge University Press.

VERRON, J. & LE PROVOST, C. 1985 A numerical study of quasi-geostrophic flow over isolated topography. *J. Fluid Mech.* **154**, 231–252.

VERZICCO, R., FLÓR, J.B., VAN HEIJST, G.J.F. & ORLANDI, P. 1995 Numerical and experimental study of the interaction between a vortex dipole and a circular cylinder. *Exp. Fluids* **18** (3), 153–163.

VIÚDEZ, A. 2019 Azimuthal-mode solutions of two-dimensional Euler flows and the Chaplygin–Lamb dipole. *J. Fluid Mech.* **859**, R1.

ZABUSKY, N.J. & MCWILLIAMS, J.C. 1982 A modulated point-vortex model for geostrophic, β-plane dynamics. *Phys. Fluids* **25** (12), 2175–2182.

ZAVALA SANSÓN, L. 2002 Vortex–ridge interaction in a rotating fluid. *Dyn. Atmos. Oceans* **35** (4), 299–325.

ZAVALA SANSÓN, L. 2010 Solutions of barotropic trapped waves around seamounts. *J. Fluid Mech.* **661**, 32–44.

ZAVALA SANSÓN, L. 2019 Nonlinear and time-dependent equivalent-barotropic flows. *J. Fluid Mech.* **871**, 925–951.

ZAVALA SANSÓN, L., BARBOSA AGUIAR, A.C. & VAN HEIJST, G.J.F. 2012 Horizontal and vertical motions of barotropic vortices over a submarine mountain. *J. Fluid Mech.* **695**, 173–198.

ZAVALA SANSÓN, L. & VAN HEIJST, G.J.F. 2000 Interaction of barotropic vortices with coastal topography: laboratory experiments and numerical simulations. *J. Phys. Oceanogr.* **30** (9), 2141–2162.

ZAVALA SANSÓN, L. & VAN HEIJST, G.J.F. 2002 Ekman effects in a rotating flow over bottom topography. *J. Fluid Mech.* **471**, 239–255.

ZAVALA SANSÓN, L. & VAN HEIJST, G.J.F. 2014 Laboratory experiments on flows over bottom topography. In *Modeling Atmospheric and Oceanic Flows: Insights from Laboratory Experiments and Numerical Simulations* (ed. T. von Larcher & P.D. Williams). Wiley.

ZAVALA SANSÓN, L., VAN HEIJST, G.J.F. & BACKX, N.A. 2001 Ekman decay of a dipolar vortex in a rotating fluid. *Phys. Fluids* **13** (2), 440–451.

ZAVALA SANSÓN, L., VAN HEIJST, G.J.F. & DOORSCHOT, J.J.J. 1999 Reflection of barotropic vortices from a step-like topography. *Il Nuovo Cimento* **22** (6), 909–930.

ZHAO, B., CHIEUSSE-GÉRARD, E. & FLIERL, G. 2019 Influence of bottom topography on vortex stability. *J. Phys. Oceanogr.* **49** (12), 3199–3219.